

Article

Investigation on the Flow in a Rotor-Stator Cavity with Centripetal Through-Flow [†]

Bo Hu ^{*}, Dieter Brillert, Hans Josef Dohmen and Friedrich-Karl Benra 

Department of Mechanical Engineering, University of Duisburg-Essen, 47057 Duisburg, Germany; dieter.brillert@uni-due.de (D.B.); hans-josef.dohmen@uni-due.de (H.J.D.); friedrich.benra@uni-due.de (F.-K.B.)

^{*} Correspondence: bo.hu.1987@stud.uni-due.de; Tel.: +49-203-379-1703

[†] This paper is an extended version of our paper in Proceedings of the European Turbomachinery Conference ETC12, 2017, Paper No. 97.

Academic Editor: Claus Sieverding

Received: 31 July 2017; Accepted: 6 October 2017; Published: 19 October 2017

Abstract: Daily and Nece distinguished four flow regimes in an enclosed rotor-stator cavity, which are dependent on the circumferential Reynolds number and dimensionless axial gap width. A diagram of the different flow regimes including the respective mean profiles for both tangential and radial velocity was developed. The coefficients for the different flow regimes have also been correlated. In centrifugal pumps and turbines, the centripetal through-flow is quite common from the outer radius of the impeller to the impeller eye, which has a strong influence on the radial pressure distribution, axial thrust and frictional torque. The influence of the centripetal through-flow on the cavity flow with different circumferential Reynolds numbers and dimensionless axial gap width is not sufficiently investigated. It is also quite important to convert the 2D Daily and Nece diagram into 3D by introducing the through-flow coefficient. In order to investigate the impact of the centripetal through-flow, a test rig is designed and built up at the University of Duisburg-Essen. The design of the test rig is described. The impact of the above mentioned parameters on the velocity profile, pressure distribution, axial thrust and frictional torque are presented and analyzed in this paper. The 3D Daily and Nece diagram introducing the through-flow coefficient is also organized in this paper.

Keywords: rotor-stator cavity; centripetal through-flow; axial thrust; frictional torque

1. Introduction

In radial pumps and turbines, the leakage flow (centripetal through-flow) is quite common from the outer radius of the impeller to the impeller eye, which has a major impact on the pressure distribution, axial thrust (F_a) and frictional torque. Von Kármán [1] and Cochran [2] gave a solution of the ordinary differential equation for the steady, axisymmetric, incompressible flow. Daily and Nece [3] examined the flow of an enclosed rotating disk both analytically and experimentally. They distinguished the four flow regimes, shown in Figure 1, by correlating different empirical equations of the moment coefficients. Kurokawa et al. [4–6] studied the cavity flow with both centrifugal and centripetal through-flow. Schlichting and Gersten [7] organized an implicit relation based on the results of Goldstein [8] for the moment coefficient under turbulent flow conditions. Poncet et al. [9] studied the centripetal through-flow in a rotor-stator cavity and obtained an equation of the core swirl ratio K based on the local flow rate coefficient (C_{qr}) for Batchelor type flow [10]. For Batchelor type flow, the centrifugal disk boundary layer and the centripetal wall boundary layer are separated by a central core. Debuchy et al. [11] derived an explicit equation for K which is valid over a wide range of C_{qr} . Launder et al. [12] provided a review of the current understanding of instability pattern that are created in rotor-stator cavities leading to transition and eventually turbulence. Recent experimental

investigations up to circumferential Reynolds numbers $Re = 5 \times 10^8$ with and without through-flow have been conducted by Coren et al. [13], Long et al. [14] and Barabas et al. [15]. The scope of the present study is shown in Figure 1.

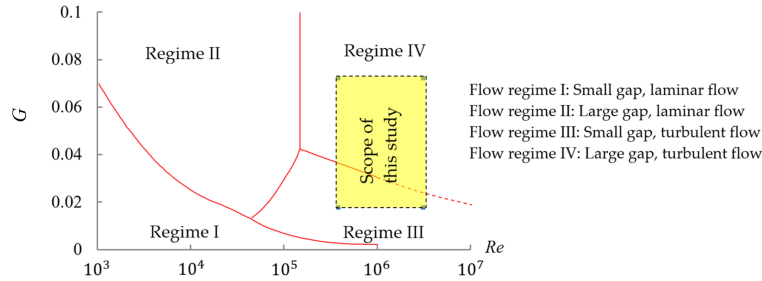


Figure 1. Flow regimes according to Daily and Nece [3].

The main dimensions of the rotor-stator cavity are illustrated in Figure 2. This study focuses on the influence of non-pre-swirl centripetal through-flow on the cavity flow. Based on the results from previous studies, C_D' (through-flow coefficient) may have a large influence on the moment coefficient, noted as C_M . Uncertainties still exist in the effect of C_D' on C_M with different values of Re and G (dimensionless axial gap). This study is aimed to provide more results to increase the dataset and to better understand the influence of above parameters on C_p (pressure coefficient), C_F (axial thrust coefficient) and C_M . The definitions of the significant dimensionless parameters in this study are given in Equations (1a)–(1k).

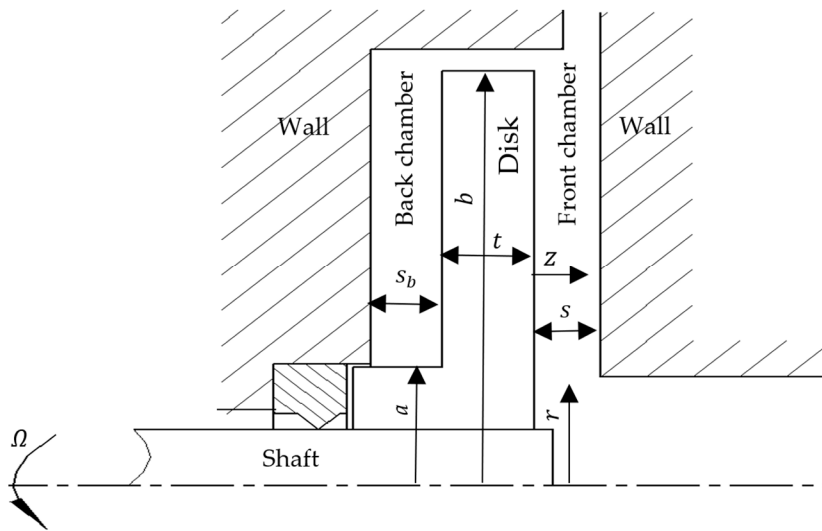


Figure 2. Main dimensions of the test rig. a : Hub radius; b : outer radius of the disk; r : radial coordinate; s : axial gap of the front chamber; s_b : axial gap of the back chamber; t : thickness of the disk; z : axial coordinate.

$$Re = \frac{\Omega \cdot b^2}{\nu} \tag{1a}$$

$$Re_\varphi = \frac{\Omega \cdot r^2}{\nu} \tag{1b}$$

$$G = \frac{s}{b} \tag{1c}$$

$$C_D' = \frac{\dot{m}}{\mu \cdot b} \tag{1d}$$

$$C_F = \int_a^b \frac{2 \cdot \pi \cdot (p_b - p) \cdot r \, dr}{\rho \cdot \omega^2 \cdot b^4} \tag{1e}$$

$$C_{qr} = \frac{Q \cdot Re_\varphi^{0.2}}{2 \cdot \pi \cdot \Omega \cdot r^3} \tag{1f}$$

$$\zeta = \frac{z}{s} \tag{1g}$$

$$x = \frac{r}{b} \tag{1h}$$

$$C_M = \frac{2 \cdot |M|}{\rho \cdot \Omega^2 \cdot b^5} \tag{1i}$$

$$p^* = \frac{p}{\rho \cdot \Omega^2 \cdot b^2} \tag{1j}$$

$$C_p = p^*(x = 1) - p^*(x) \tag{1k}$$

2. Theoretical Analysis

In this study, the values of Q (volumetric through-flow rate), C_D' and C_{qr} are negative for centripetal through-flow. Using a two-component Laser Doppler Anemometer (LDA) system, Poncet et al. [9] correlated Equation (2a) to evaluate the core swirl ratio K (the ratio of the angular velocity of the fluid to that of the disk at $\zeta = 0.5$) with centripetal through-flow when $C_{qr} \geq -0.2$. Debuchy et al. [11] determined Equation (2b) to calculate the values of K for a wider range $C_{qr} \geq -0.5$ with a two-component LDA system. The results from Equation (2b) are smaller than those from Equation (2a) at large values of $|C_{qr}|$, compared in Figure 3.

$$K = 2 \cdot (-5.9 \cdot C_{qr} + 0.63)^{\frac{5}{7}} - 1 \tag{2a}$$

$$K = \left[\frac{-8.85 \cdot C_{qr} + 0.5}{e^{(-1.45C_{qr})}} \right]^{\frac{5}{4}} \tag{2b}$$

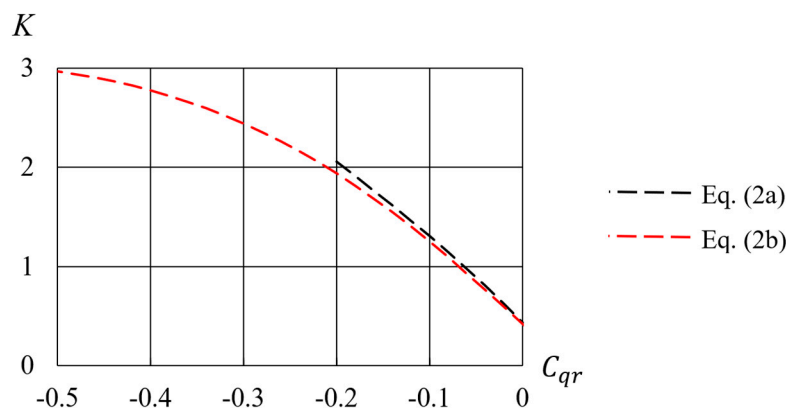


Figure 3. Comparison of results from Equations (2a) and (2b). K : core swirl ratio at $\zeta = 0.5$; C_{qr} : local flow rate coefficient; Eq: equation.

A number of studies, such as those by Kurokawa et al. [6], Poncet et al. [9], Coren et al. [13], and Barabas et al. [15], show that the pressure distribution along the radius of the disk can be

estimated with the core swirl ratio K both with and without through-flow. Will et al. [16–18] determined Equation (3) to evaluate the pressure distribution along the radius of the disk for the incompressible, steady flow. It is obtained directly from the radial momentum equation when the turbulent shear stress is neglected. In a rotor-stator cavity, the cross sectional area changes in radial direction. Consequently, the pressure must also change since the mean velocity changes in radial direction according to the continuity equation.

$$\frac{\partial p}{\partial r} = \rho \left(\frac{v_\varphi^2}{r} - v_r \frac{\partial v_r}{\partial r} \right) = \rho \cdot K^2 \cdot \Omega^2 \cdot r + \frac{\rho \cdot Q^2}{4 \cdot \pi^2 \cdot s^2 \cdot r^3} \quad (3)$$

The difference of the force on both sides of the disk is the main source for axial thrust, noted as F_a , calculated with Equation (4a). F_{af} (force on the front surface of the disk; calculated with Equation (4b)) and C_{Ff} (C_F on the front surface) respectively represent the force and the thrust coefficient on the front surface of the disk (in the front chamber, shown in Figure 2), while F_{ab} (force on the back surface of the disk; calculated with Equation (4c)) and C_{Fb} are those on the back surface of the disk (in the back chamber). a and p_b represent the radius of the hub (see Figure 2) and the pressure at $x = 1$, respectively. The back chamber ($G = 0.072$), shown in Figure 2, is supposed to be an enclosed cavity. The values of C_{Fb} (C_F on the back surface) are obtained when $C_{D'} = 0$ and the axial gaps of both cavities have the same size for different Re (under that condition $C_{Ff} = C_{Fb}$). After obtaining those values, the values of C_{Ff} with different values of $C_{D'}$ can be calculated with Equation (5).

$$F_a = F_{ab} - F_{af} \quad (4a)$$

$$F_{af} = \pi \cdot p_b \cdot b^2 - C_{Ff} \cdot \rho \cdot \Omega^2 \cdot b^4 \quad (4b)$$

$$F_{ab} = \pi \cdot p_b \cdot (b^2 - a^2) - C_{Fb} \cdot \rho \cdot \Omega^2 \cdot (b^4 - a^4) \quad (4c)$$

$$C_{Ff} = \frac{F_a + C_{Fb} \cdot \rho \cdot \Omega^2 (b^4 - a^4) + \pi p_b a^2}{\rho \cdot \Omega^2 \cdot b^4} \quad (5)$$

3. Test Rig Design and Experimental Set-Up

The design of the test rig is shown in Figure 4. The cross section of the test rig is depicted in Figure 4a. The centripetal through-flow (volumetric through-flow rate Q), shown by the black arrows in Figure 4a, is supplied with water by a pump system. The view along the “A” direction is sketched in Figure 4b. The shaft sealing at the back cavity is depicted in Figure 4c ($r_{seal} = 10$ mm). A picture of the test rig is shown in Figure 4d. The shaft is driven by an electric motor. A frequency converter is used to adjust the speed of rotation (0–2500/min) with the absolute uncertainty of 7.5/min. In this study, only the axial gap of the front chamber is changed by installing six sleeves with different length. There are 24 channels in the guide vane (instead of entirely open at the periphery) to get more uniform centripetal through-flow, shown in Figure 4b. The area of each channel is 4×10^{-6} m². In this study, the channels in the guide vane are radial directed (see Figure 4b). Other parameters of the experiments in this study are given in Table 1. The transducers in the test rig include two pressure transducers (36 pressure tubes), a torque transducer and three tension compression transducers. A thrust plate is fixed by a ball bearing and a nut from both sides to convey the axial thrust to the tension compression transducers. A linear bearing is used to minimize the frictional resistance during the axial thrust measurements. During the measurements of axial thrust, the calibrations of the axial thrust transducers are performed when changing the axial gap width of the front chamber. When measuring the torque, the values of the shaft without the disk rotating at different speeds of rotation are subtracted. The measured R_z of the disk is 1 μ m. The values of R_z on all the other surfaces of the test rig are below 1.6 μ m.

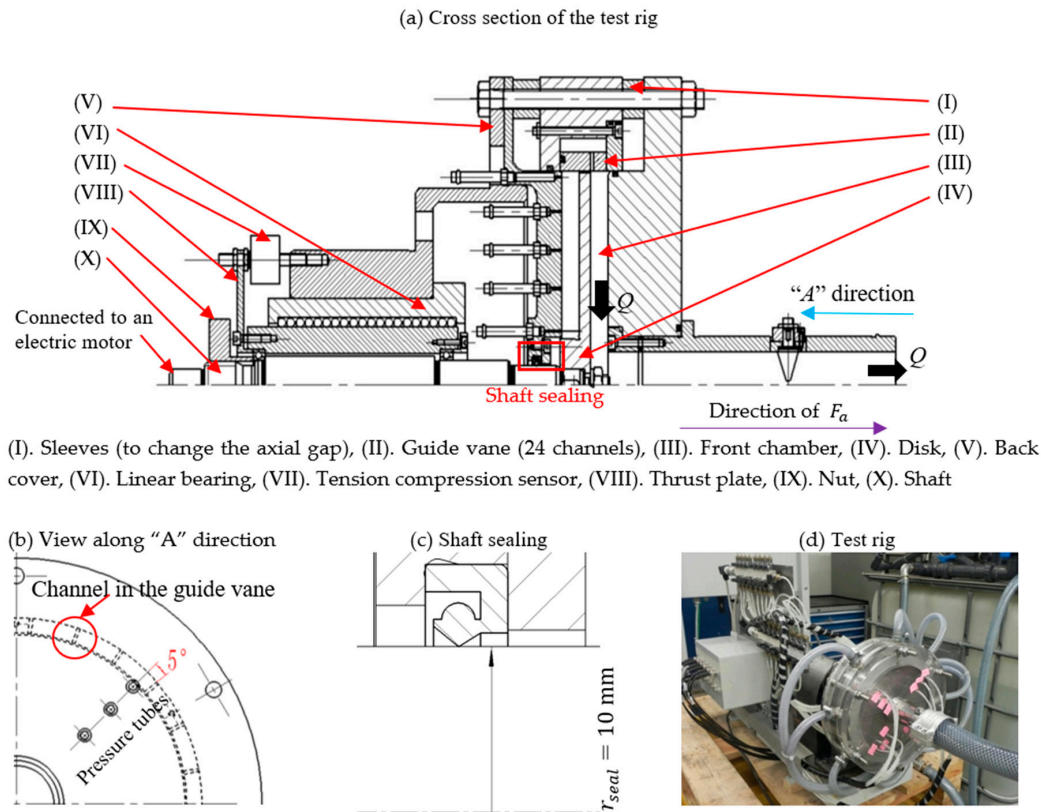


Figure 4. Test rig design. F_a : axial thrust; r_{seal} : radius of shaft seal.

Table 1. Parameters of the experiments.

b (mm)	n (/min)	Q (m^3/s)	s (mm)	s_b (mm)	a (mm)	t (mm)
110	0~2500	$-5.56 \times 10^{-4} \sim 0$	2~8	8	23	10

n : speed of rotation; Q : volumetric through-flow rate.

The measurements of the axial thrust include two steps. The cavities for each step are depicted in Figure 5. The first step is to measure the axial force imposed by the drive end of the motor when the shaft without the disk is rotating at different speed of rotation in the air. For the second step, all the results are modified by subtracting above values obtained at the first step according to the speed of rotation. The shaft head in Figure 5b is considered as a part of front surface (with the area of $\Omega \cdot b^2$). The geometry of the nut is ignored. Then, the values of thrust coefficient on a single surface can be calculated with Equation (5).

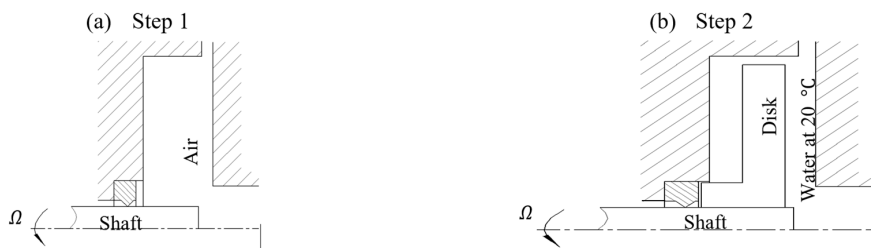


Figure 5. Cavities to measure the axial thrust.

The relative error, noted as e_T , of the pressure transducers is 1% (full scale (FS)). The value of e_T for the torque transducer is 0.1% (FS). The value of e_T for the axial thrust transducers is 0.5% (FS). All the experimental results are the ensemble average of 1000 samples. The uncertainties of the measured results, noted as ΔN , are the differences between the real values and the measured values. They are estimated with the root sum squared method. The uncertainties are calculated with Equation (6). N_T is the uncertainty due to the transducers. N_D is the uncertainty due to the data acquisition system. The measuring range (M_r) of the torque meter is 0~10 Nm. The measured range of the pressure transducer is 0~2.5 bar (absolute pressure). The measured range of the thrust transducers is -100~100 N. The input voltage signals are the following ranges: 0~10 V for the pressure transducers and the torque transducer, -10 V~10 V for the axial thrust transducers. The absolute accuracy of the data acquisition system (with NI USB-6008) is 4.28 mV in this study. The random noise and zero order uncertainty are neglected because they are very small. The distributions of the results are considered as normal distributions and the normal distribution coefficient is selected as 1.96 (95% confidence level). n_T represents the number of the transducers used to obtain one result together. To evaluate F_a and M on the front surface, the total results, the results on the back surface (obtained when $C_D' = 0$ and $s = s_b$) and the results when the shaft is rotating without disk are measured with the transducers. Hence, the measuring times to obtain one result, noted as n_M , is 3 for the axial thrust, the frictional torque (M) and Re (by measuring n). The uncertainties of the measurements are summarized in Table 2.

$$\Delta N = \sqrt{N_T^2 + N_D^2}; N_T = \frac{\sqrt{n_T \cdot n_M \cdot (e_T \cdot M_r)^2}}{1.96 \cdot \sqrt{1000}}; N_D = \frac{\sqrt{n_T \cdot n_M \cdot (e_D \cdot M_r)^2}}{1.96 \cdot \sqrt{1000}} \quad (6)$$

Table 2. Uncertainty analysis for the measurements.

	p (Bar)	F_a (N)	M (Nm)	Re	C_D'
ΔN	4.04×10^{-4}	2.43×10^{-2}	3.00×10^{-4}	9.01×10^4	4.1
n_T	1	3	1	1	1
n_M	1	3	3	3	1

ΔN : uncertainty of the measured results; n_T : number of transducers; n_M : measuring times to obtain one result; p : pressure; M : frictional torque; Re : global circumferential Reynolds number; C_D' : through-flow coefficient.

4. Numerical Simulation

To predict the cavity flow, numerical simulations are carried out using the ANSYS CFX 14.0 code [15]. There are 24 channels in the guide vane. Considering the axial symmetry of the problem, a segment (15 degree) of the whole domain is modeled and a rotational periodic boundary condition is applied. Structured meshes are generated with ICEM 14.0. The domain for the numerical simulation when $G = 0.072$ is depicted with yellow color in Figure 6. The simulation type is set as steady state. Barabas et al. [15] found that the simulation results from the shear stress transport (SST) $k - \omega$ turbulence model in combination with the scalable wall functions are in good agreement with the measured pressure in a rotor-stator cavity with air. The deviations of the pressure measurement are less than 1%. Hence, in this study, the same turbulence model and wall functions are used. The boundary conditions at the inlet and at the outlet are pressure inlet and mass flow outlet, respectively. The values of the pressure at the inlet are set according to the pressure sensor at the pump outlet. The convergence criteria for all the numerical simulations are set as 10^{-5} in maximum type. The turbulent numeric is set as second order upwind. The maximum value of y^+ in all the simulation models is 13.4.

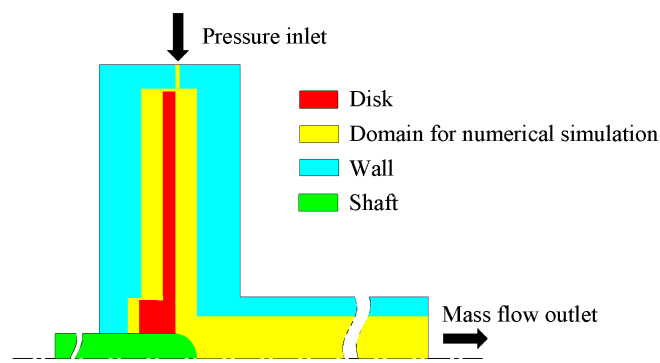


Figure 6. Domain for numerical simulation when $G = 0.072$.

5. Results and Discussion

5.1. Simulation Results of Velocity Distributions

The velocity profiles are sensitive to the boundary condition at the inlet. The profiles in the front chamber are discussed in this part because there is a small jet flow through each channel in the guide vane. All the velocities are made dimensionless by dividing them by $\Omega \cdot b$. The values of V_z are positive when they have a direction from the disk to the wall. The velocity profiles at three radial positions for $Re = 1.9 \times 10^6$ and $G = 0.072$ (wide gap) are shown in Figure 7. The dimensionless radial velocities are not exactly zero in the central cores, shown in Figure 7a–c. From the distribution of tangential velocity, there are central cores at all the investigated radial positions where the values of V_ϕ are almost constant, shown in Figure 7d–f. At $x = 0.955$ and $x = 0.79$, the values of the tangential velocity are smaller at $\zeta = 0.5$ when $|C_D'|$ increase from 1262 to 3787 and 5050, depicted in Figure 7d,e. The profiles are special, because according to the former results (such as from Poncet et al. [9] and Debuchy et al. [11]), the increase of $|C_D'|$ will result in an increase of the core swirl ratio K for centripetal through-flow. Then, the tangential velocity should increase instead of decrease. Probably this can be attributed to the jet flow through the channel at the inlet, which is stronger at large $|C_D'|$. At $x = 0.955$, the values of $|V_z|$ become smaller for larger $|C_D'|$ in general, shown in Figure 7g. The direction of V_z is from the disk towards the wall for $|C_D'| = 0$ and $|C_D'| = 1262$ at $x = 0.955$, while it is from the wall towards the disk at $|C_D'| = 3787$ and $|C_D'| = 5050$. There are axial circulations of the fluid in the front chamber. The directions of the axial circulations, however, are strongly influenced by the values of $|C_D'|$, depicted in Figure 7g–i.

The velocity profiles at the three radial coordinates for $Re = 1.9 \times 10^6$ and $G = 0.018$ (small gap) are shown in Figure 8. The dimensionless radial velocities V_r vary along ζ , shown in Figure 8a–c. The values of V_r decrease with the increase of $|C_D'|$ in general. The tangential velocity V_ϕ decreases constantly with the increase of ζ , which is the characteristic of the regime III, shown in Figure 8d–f. At $x = 0.955$ and $x = 0.79$, the values of tangential velocity are much smaller at large $|C_D'|$, shown in Figure 8d. The reason is that the impact of the jet flow at the inlet becomes greater for smaller G . The profiles of V_z are quite different at $x = 0.955$ in Figure 8g, compared with those in Figure 7g. The values of V_z are less than those from Figure 7h,i. The results of V_z indicate that the axial circulations of fluid are sensitive to the values of G .

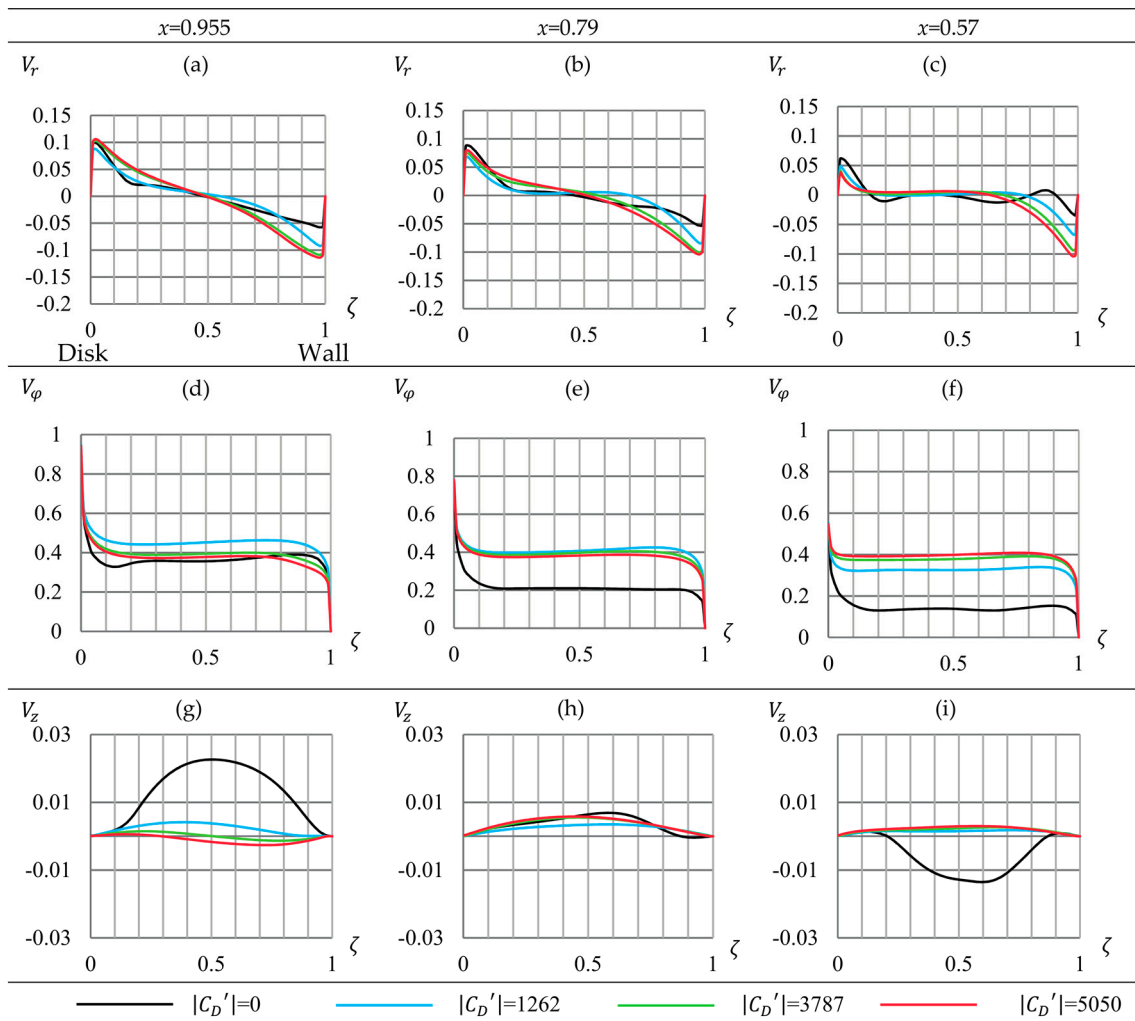


Figure 7. Velocity profiles for $Re = 1.9 \times 10^6$ and $G = 0.072$ (wide gap). G : dimensionless axial gap.

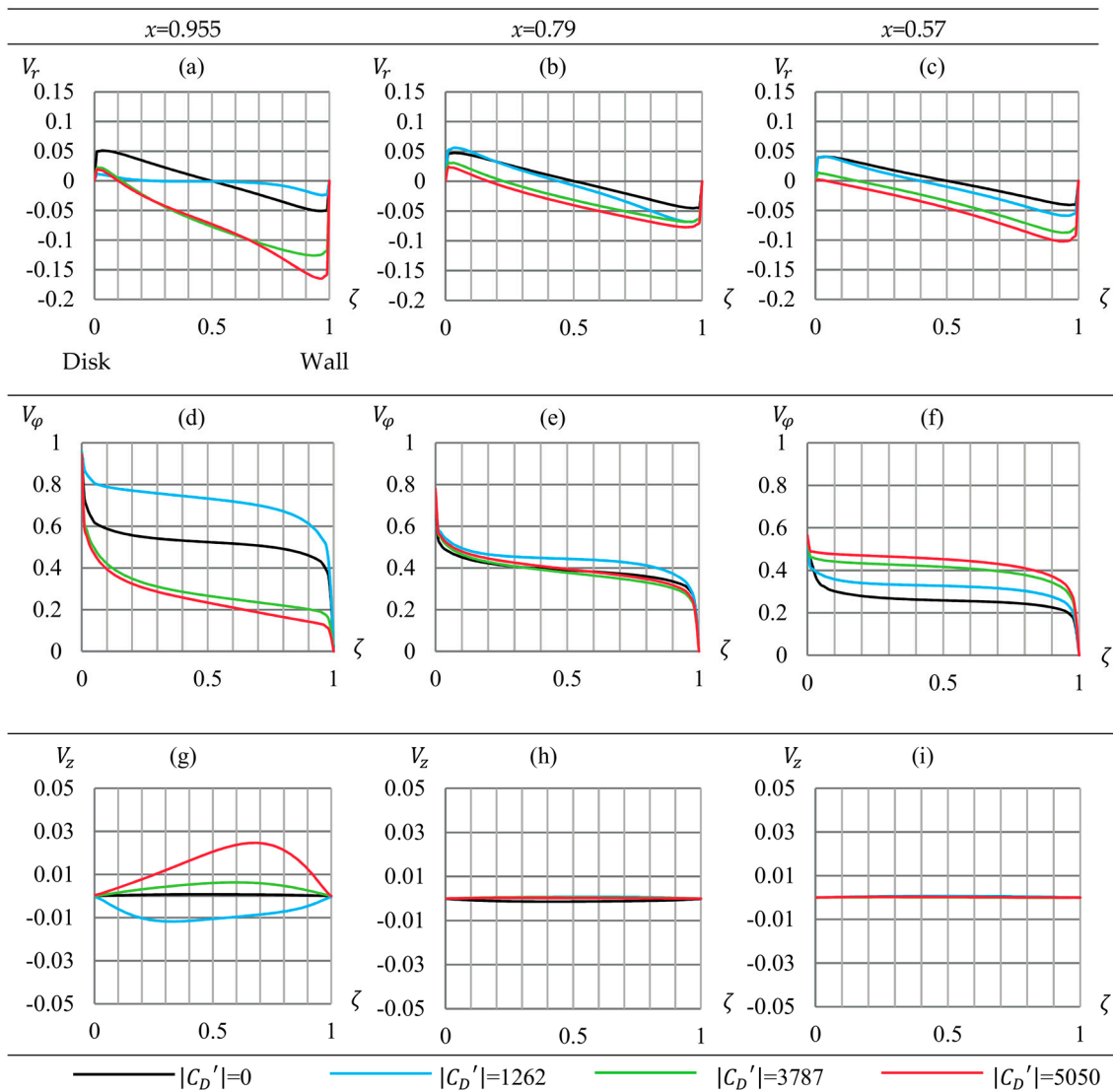


Figure 8. Velocity profiles for $Re = 1.9 \times 10^6$ and $G = 0.018$ (small gap).

5.2. Pressure Distributions

Due to the construction of the geometry, there is no pressure tube at $x = 1$. The closest tube is at $x = 0.955$. The pressure values at $x = 1$ (reference pressure) are taken from numerical simulation. Since the values of p from numerical simulation at $x = 0.955$ are close to those from experiments, the small errors are neglected.

The pressure coefficient C_p are positive values because the pressure drops towards the shaft. In Figure 9, the values of C_p are plotted versus the dimensionless radial coordinates for three values of Re and G . The experimental results show that the values of C_p increase with increasing $|C_D'|$. The values of C_p decrease with the increase of Re and G in general. When $Re = 1.9 \times 10^6$ and $Re = 2.79 \times 10^6$, the uncertainties of the C_p are respectively 2.7×10^{-4} and 1.3×10^{-4} , which are very small compared with the measured results. Hence, they are neglected in Figure 9d–i.

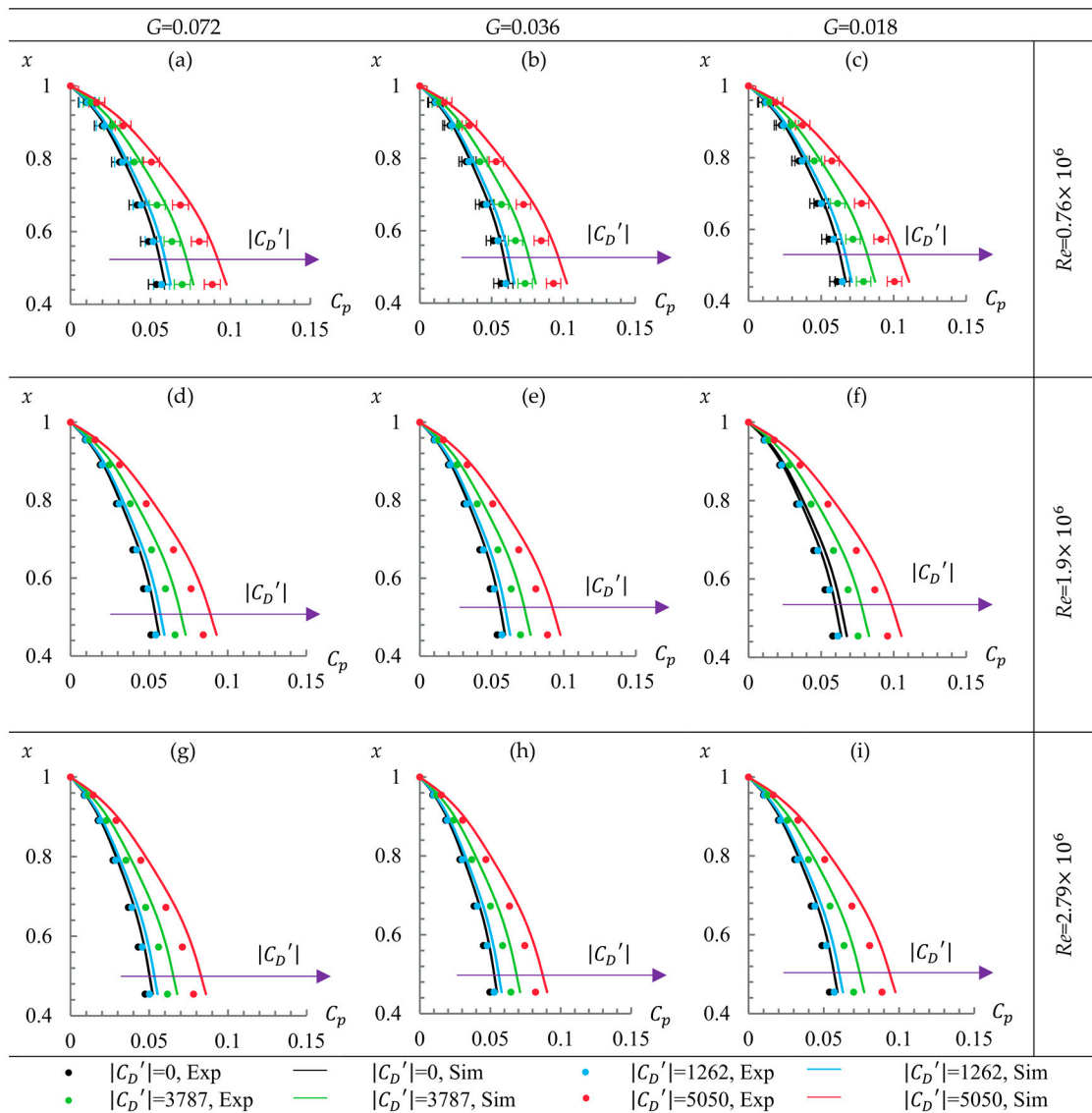


Figure 9. Influence of C_D' on C_p (pressure coefficient) in dependence of Re and G .

5.3. Axial Thrust Coefficient

Based on the axial thrust measurements (direction of the axial thrust see Figure 4a), a correlation for C_{Ff} is determined, given in Equation (7). The results from Equation (7) are consistent with the experimental results, plotted in Figure 10. With the increase of $|C_D'|$, the values of C_{Ff} increase, which can be attributed to the drop of p . The values of C_{Ff} are smaller for higher values of G and Re .

$$C_{Ff} = \left[6.6 \cdot 10^{-3} \cdot \ln(Re) - 0.113 \right] \cdot e^{(1.2 \cdot 10^{-4} \cdot |C_D'|)} \cdot [0.122 \cdot \ln(G) - 0.67] \quad (7)$$

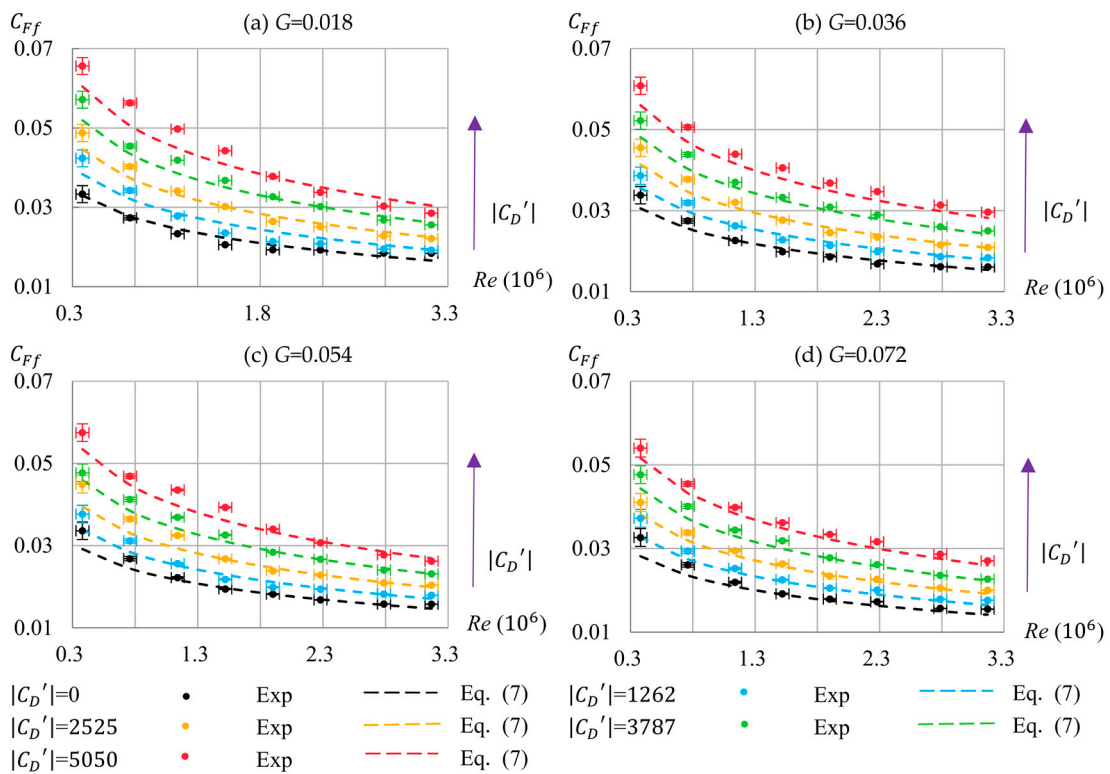


Figure 10. Mean C_{Ff} - $C_{D'}$ curves in dependence of Re and G . C_F : axial thrust coefficient; C_{Ff} : C_F on the front surface.

5.4. The 3D Daily and Nece Diagram

The typical tangential velocity profiles for regime III (merged disk boundary layer and wall boundary layer) and regime IV (separated disk boundary layer and wall boundary layer) are given in Figure 11.

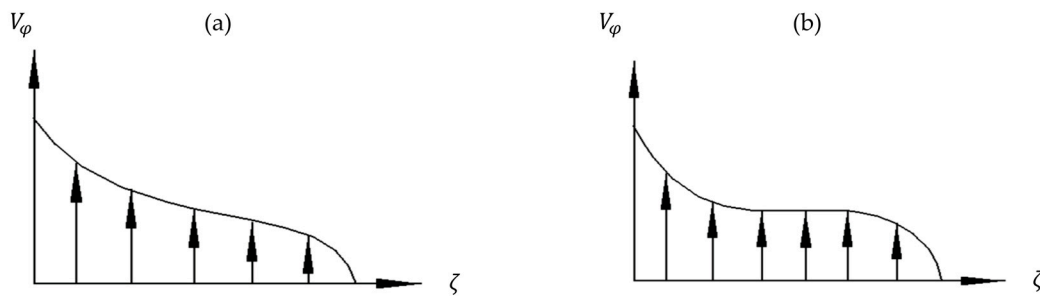


Figure 11. Typical tangential velocity profiles for: (a) regime III and (b) regime IV.

Based on the simulation results of the tangential velocity, part of the Daily and Nece diagram (see Figure 1) is extended into 3D by distinguishing the tangential velocity profiles (see Figure 11) at $x = 0.955$, $x = 0.79$ and $x = 0.57$. The scope of this study is the following parameter ranges: $|C_{D'}| \leq 5050$, $0.38 \times 10^6 \leq Re \leq 3.17 \times 10^7$ and $0.018 \leq G \leq 0.072$. They are categorized into two regimes, namely regime III (below the distinguishing lines) and regime IV (above the distinguishing lines). Currently, five distinguishing lines are found for different $|C_{D'}|$ shown in Figure 12b. The distinguishing line at $C_{D'} = 0$ is almost equal to that from Daily and Nece [3]. The distinguishing lines become steeper for higher values of $|C_{D'}|$. The approximate distinguishing surface is drawn through the lines, shown in Figure 12a. Below and above the surface are regime III and regime IV, respectively. Near the

distinguishing surface, there is a mixing zone where regime III and regime IV coexist in the front chamber. In this study, it is not plotted in Figure 12.

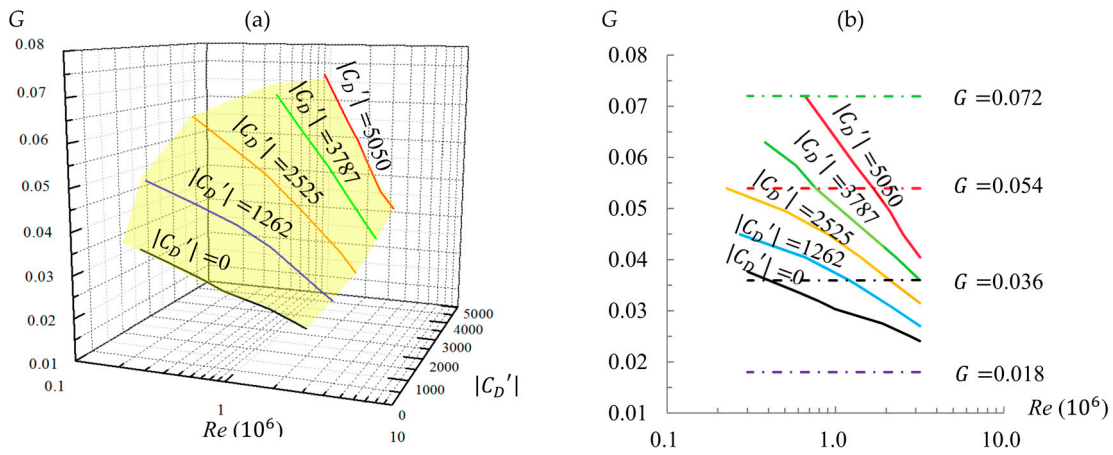


Figure 12. Part of the 3D Daily and Nece diagram: (a) Distinguishing surface and (b) Distinguishing lines.

5.5. Moment Coefficient

According to the experimental results from Han et al. [19], the moment coefficient on the cylinder surface of the disk ($C_{M_{cyl}}$) can be estimated with Equation (8) for smooth disks.

$$C_{M_{cyl}} = \frac{2 \cdot |M_{cyl}|}{\rho \cdot \Omega^2 \cdot b^5} = \frac{0.084 \cdot \pi \cdot t}{b \cdot \left(1g \frac{\Omega \cdot b^2}{\nu}\right)^{1.5152}} \tag{8}$$

When $C_{D'} = 0$, the values of C_M for $G = 0.018$ (regime III) and $G = 0.072$ (regime IV) are compared in Figure 13a,b, respectively. The differences between the experimental results and those from the correlations by Daily and Nece [3] for both regime III and regime IV, are colossal. k_s is the equivalent surface roughness, defined in Equation (11). According to Schlichting et al. [7], k_{sl} (the limitation for hydraulic smooth) wall can be estimated with Equation (12). The disk therefore can be considered hydraulic smooth when $R_z \leq 38.2 \mu\text{m}$. To explain the wide gap, the results for a rougher disk ($R_z = 22 \mu\text{m}$) are also plotted for comparison. The results are much closer to those from the equation by Daily and Nece [3]. Hence, the differences can be attributed to the difference of surface roughness. Equations (9) and (10) are therefore determined to satisfy the experimental results ($R_z = 1 \mu\text{m}$ for the disk).

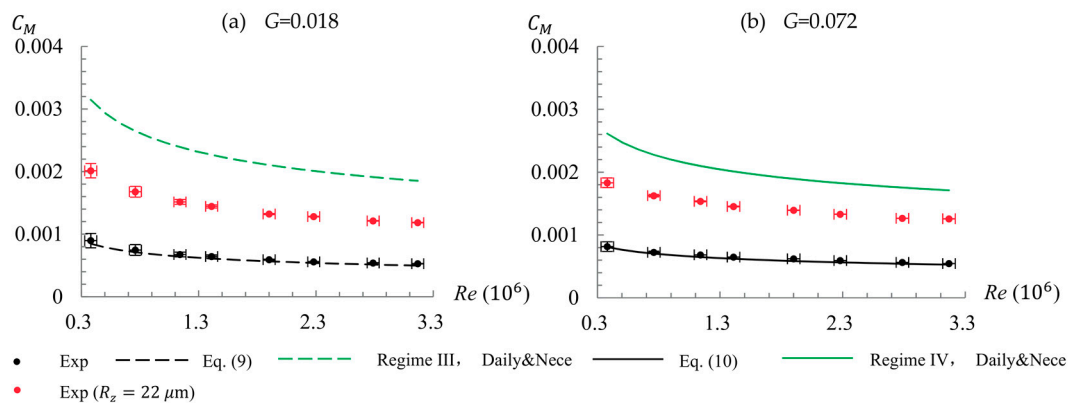


Figure 13. Comparison of the results of C_M (moment coefficient) for $G = 0.018$ and $G = 0.072$ at $C_{D'} = 0$.

$$C_{M3} = 0.011 \cdot G^{-\frac{1}{6}} \cdot Re^{-\frac{1}{4}} \cdot [e^{(0.8 \cdot 10^{-4} \cdot |C_D'|)}] \tag{9}$$

$$C_{M4} = 0.014 \cdot G^{\frac{1}{10}} \cdot Re^{-\frac{1}{5}} \cdot [e^{(0.46 \cdot 10^{-4} \cdot |C_D'|)}] \tag{10}$$

$$k_s = \frac{\pi \cdot \varepsilon}{8} \cdot r \cdot \varepsilon = 0.978 \cdot R_z \tag{11}$$

$$k_{sl} = \frac{100 \cdot \nu}{(1 - K) \cdot r \cdot \Omega} \tag{12}$$

To introduce the influence of C_D' on the moment coefficient, the results of C_M from both the experiments and the equations are plotted versus Re in Figure 14. With the increase of Re , the flow regime may change from regime III to regime IV (see the distinguishing lines in Figure 12). For $G = 0.018$ and $G = 0.036$, most of the flow regimes are regime III and the results are close to those from Equation (9) in general, shown in Figure 14a,b. The flow regimes change from regime III to regime IV with the increase of Re for $|C_D'| = 0$ and $|C_D'| = 1262$ at $G = 0.036$ in Figure 14b. For $G = 0.054$ and $G = 0.072$, most of the flow regimes are regime IV and the results are close to those from Equation (10) in general, depicted in Figure 14c,d. The results of C_M from the equations are in good agreement with those from experiments. The values of C_M increase with the increase of $|C_D'|$, while decrease with the increase of Re . At large values of Re , the impact of C_D' on C_M becomes lesser. At the same values of $|C_D'|$, the intersection points of the curves from Equation (9) and those from Equation (10) are close to those in Figure 12b. The difference can be attributed to the existence of the mixing zone.

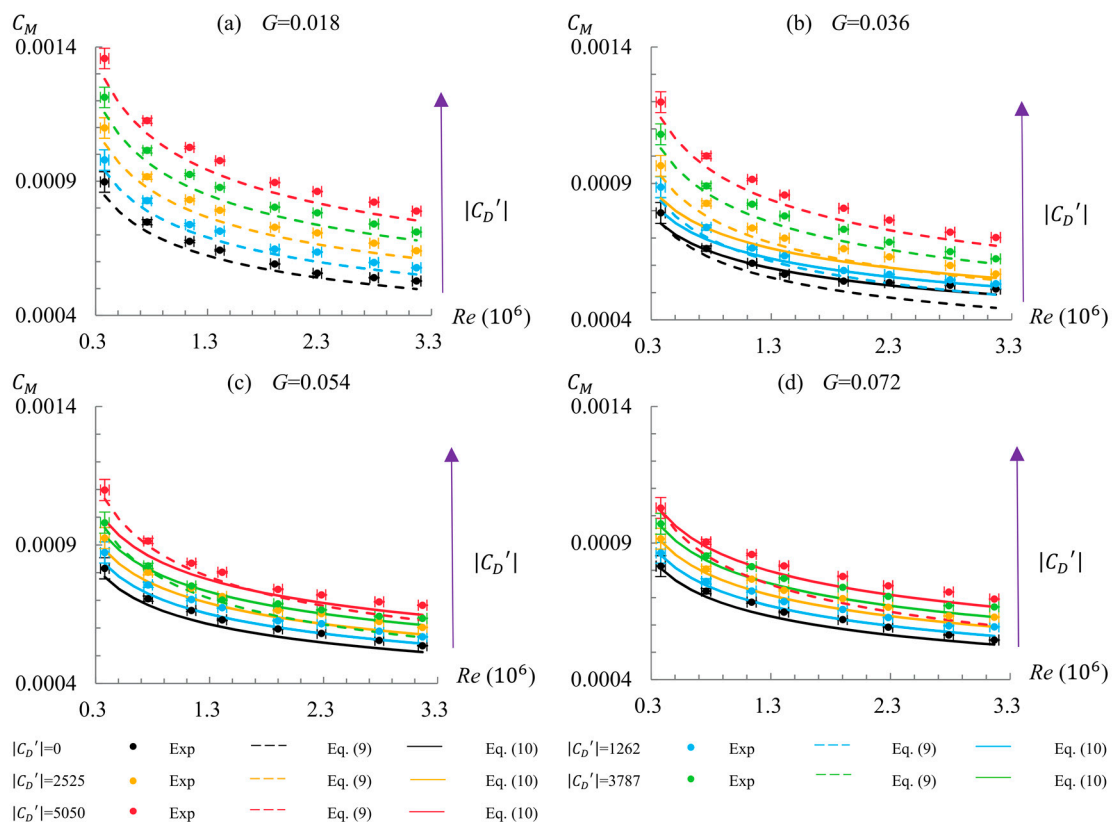


Figure 14. Curves for C_M in dependence of C_D' for different values of Re and G .

The results from Equations (9) and (10) at the distinguishing lines should be equal. The results of C_{M3}/C_{M4} (C_M for regime III/ C_M for regime IV) for a non-dimensioned gap width G at the distinguishing lines (see Figure 12b) are presented in Figure 15. The differences, attributed to the

existence of the mixing zone, are less than 4%. The results indicate that the distinguishing lines (in Figure 12), Equations (9) and (10) are reasonable.

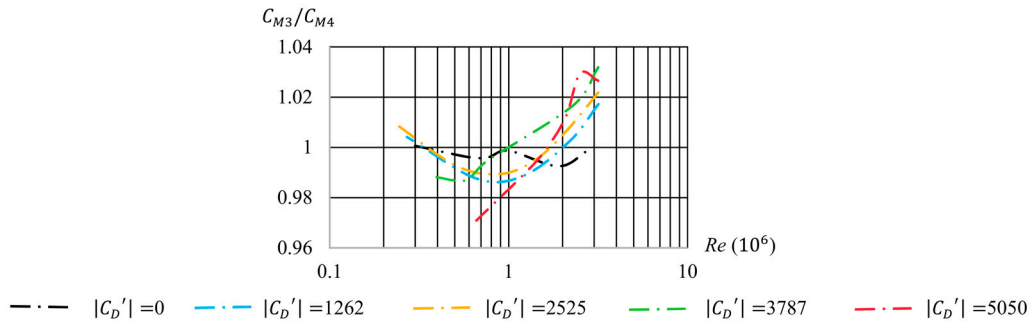


Figure 15. Results of C_{M3}/C_{M4} (C_M for regime III/ C_M for regime IV) at the distinguishing lines.

An example is provided on the applications of the results in this paper. Shi et al. [20] studied the axial thrust of a single stage well pump based on both numerical simulation and experiments. The pressure acting at the impeller is shown in Figure 16a. Based on Equation (7), the thrust coefficient at surface 1 and surface 2 can be calculated when the leakage flow is estimated. The volumetric leakage through-flow rate is considered as 5% of the flow rate of the pump. The force at the impeller eye (at surface 3) with numerical simulation. Then, the axial thrust of the impeller can be calculated when the axial force of the shaft is estimated. They predicted the force on all the surfaces of the impeller and the shaft to calculate the axial thrust. The axial force of the shaft is obtained at different flow rate from the simulation results by Shi et al. [20]. The maximum difference between their simulation results and measurements of the axial thrust is 5.9%. The values of $F_{ab} - F_{af}$ are plotted versus C_D' in Figure 16b. The experimental results of $F_{ab} - F_{af}$ are obtained by subtracting the forces on the rest of the surfaces (from numerical simulation). The results from Equation (7) are in better agreement with the experimental results than those from the equation by Kurokawa et al. [4] when C_D' ranges from 1150 to 4630.

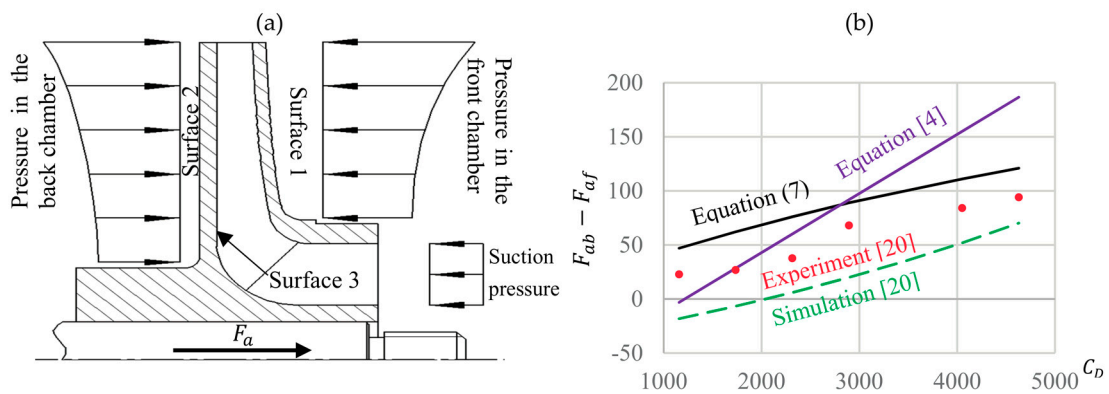


Figure 16. Axial thrust in a centrifugal single stage well pump [20]: (a) Pressure distribution and (b) Comparison of $F_{ab} - F_{af}$ [20]. F_{ab} : force on the back surface of the disk; F_{af} : force on the front surface of the disk.

There are still some limitations of this work. The results and correlations are limited to non-pre-swirl centripetal through-flow. The centripetal leakage flow in the radial pumps and turbines, however, contains a certain amount of angular momentum, which deserves further investigation. All the experimental results are obtained with the smooth disk ($R_z = 1 \mu\text{m}$). The applications of the equations are still limited because all of the results are influenced by the surface roughness of the disks. Some more

results will be presented with rough disks and the equations will be modified by introducing the impact of the surface roughness of the disks in the next step. Currently, the distinguishing lines for regime III and regime IV are obtained by evaluating the tangential flow component based on numerical simulation. This will be put on an experimental level by measuring the velocity components in both tangential and radial direction with a Laser Doppler Velocimetry (LDV) system in the future.

6. Conclusions

The influence of centripetal through-flow on the velocity, radial pressure distribution, axial thrust and frictional torque in a rotor-stator cavity with different axial gaps is illustrated to be strong.

A correlation is determined, which enables to predict the influence of G , Re and C_D' on the thrust coefficient C_F for a smooth disk ($R_z = 1 \mu\text{m}$).

For the first time, part of the 3D Daily and Nece diagram is obtained by distinguishing the tangential velocity profiles. Currently, the flow regimes are categorized into two regimes, namely regime III and regime IV. Five distinguishing lines and the approximate distinguishing surface are presented. Two correlations are determined to predict the influence of C_D' on C_M for the two regimes with good accuracy for the smooth disk ($R_z = 1 \mu\text{m}$). At the distinguishing lines, the results from the two equations are very close.

Using the equations for the axial thrust coefficient and the moment coefficient, the influence of the centripetal through-flow can be better considered when designing radial pumps and turbines with smooth impellers. Some more attention will be drawn in the future to the impact of the disk roughness. The 3D Daily and Nece diagram will be modified based on the velocity measurements with a LDV system.

Acknowledgments: This study is funded by China Scholarship Council and the chair of turbomachinery at University of Duisburg-Essen.

Author Contributions: Bo Hu, Dieter Brillert, Hans Josef Dohmen and Friedrich-Karl Benra devised and designed the experiments; Hans Josef Dohmen guided the design and the construction of the test rig; Dieter Brillert was responsible for the lab safety and the risk assessment; Friedrich-Karl Benra contributed the funds for the experiments and was supervisor during the research; Bo Hu did all the measurements and wrote the paper while Friedrich-Karl Benra reviewed the paper.

Conflicts of Interest: The authors declare no conflict of interest.

Nomenclature

Latin Symbols

a	Hub radius
b	Outer radius of the disk
C_D'	Through-flow coefficient
C_F	Axial thrust coefficient
C_{Ff}	C_F on the front surface
C_{Fb}	C_F on the back surface
C_M	Moment coefficient
$C_{M_{cyl}}$	Moment coefficient on the cylinder surface of the disk
C_{M3}	C_M for regime III
C_{M4}	C_M for regime IV
C_p	Pressure coefficient
C_{qr}	Local flow rate coefficient
e_T	Relative error of the transducer
e_D	Relative error due to the data acquisition device
F_a	Axial thrust
F_{af}	Force on the front surface of the disk
F_{ab}	Force on the back surface of the disk

G	Dimensionless axial gap
K	Core swirl ratio at $\zeta = 0.5$
k_s	Equivalent surface roughness
k_{sl}	Limitation of k_s for hydraulic smooth wall
M	Frictional torque
M_{cyl}	Frictional resistance on the cylinder surface of the disk
M_r	Measured range
\dot{m}	Mass flow rate
N_D	Uncertainty of the data acquisition system
N_T	Uncertainty of the transducer
ΔN	Uncertainty of the measured results
n	Speed of rotation
n_T	Number of transducers
n_M	Measuring times to obtain one result
p	Pressure
p_b	Pressure at $r = b$
p^*	Dimensionless pressure
Q	Volumetric through-flow rate
Re	Global circumferential Reynolds number
Re_φ	Local circumferential Reynolds number
r	Radial coordinate
r_{seal}	Radius of shaft seal
s	Axial gap of the front chamber
s_b	Axial gap of the back chamber
t	Thickness of the disk
V_r	Dimensionless radial velocity
V_z	Dimensionless axial velocity
V_φ	Dimensionless tangential velocity
x	Dimensionless radial coordinate
z	Axial coordinate

Greek Symbols

ε	Diameter of spheres
ζ	Dimensionless axial coordinate
μ	Dynamic viscosity of water
ν	Kinematic viscosity of water
ρ	Density of water
Ω	Angular velocity of the disk

Abbreviations

FS	Full scale
LDA	Laser Doppler Anemometer
LDV	Laser Doppler Velocimetry
SST	Shear Stress Transport

References

1. Kármán, T.V. Über laminare und turbulente Reibung. *Z. Angew. Math. Mech.* **1921**, *1*, 233–252. [[CrossRef](#)]
2. Cochran, W.G. The flow due to a rotating disk. *Proc. Camb. Philos. Soc.* **1934**, *30*, 365–375. [[CrossRef](#)]
3. Daily, J.W.; Nece, R.E. Chamber dimension effects on induced flow and frictional resistance of enclosed rotating disks. *J. Basic Eng.* **1960**, *82*, 217–232. [[CrossRef](#)]
4. Kurokawa, J.; Toyokura, T. Study on axial thrust of radial flow turbomachinery. In Proceedings of the 2nd International JSME Symposium Fluid Machinery and Fluid Mechanics, Tokyo, Japan, September 1972; pp. 31–40.

5. Kurokawa, J.; Toyokura, T. Axial Thrust, Disc Friction Torque and Leakage Loss of Radial Flow Turbomachinery. In Proceedings of the International Conference on Pump and Turbine Design and Development, Glasgow, UK, 1–3 September 1976.
6. Kurokawa, J.; Toyokura, T. Roughness Effects on the Flow along an Enclosed Rotating Disc. *Bull. JSME* **1978**, *21*, 1725–1732. [[CrossRef](#)]
7. Schlichting, H.; Gersten, K. *Grenzschicht-Theorie*; Springer: Berlin, Germany, 2006.
8. Goldstein, S. On the resistance to the rotation of a disc immersed in a fluid. *Proc. Camb. Philos. Soc.* **1935**, *31*, 232–241. [[CrossRef](#)]
9. Poncet, S.; Chauve, M.P.; Le Gal, P. Turbulent rotating disk flow with inward throughflow. *J. Fluid Mech.* **2005**, *522*, 253–262. [[CrossRef](#)]
10. Batchelor, G.K. Note on a class of solutions of the Navier-Stokes equations representing steady rotationally-symmetric flow. *Q. J. Mech. Appl. Math.* **1951**, *4*, 29–41. [[CrossRef](#)]
11. Debuchy, R.; Abdel Nour, F.; Bois, G. On the flow behavior in rotor-stator system with superimposed flow. *Int. J. Rotating Mach.* **2008**, *2008*, 719510. [[CrossRef](#)]
12. Launder, B.; Poncet, S.; Serre, E. Laminar, Transitional, and Turbulent Flows in Rotor-Stator cavities. *Annu. Rev. Fluid Mech.* **2010**, *42*, 229–248. [[CrossRef](#)]
13. Coren, D.; Childs, P.R.N.; Long, C.A. Windage sources in smooth-walled rotating disc systems. *Proc. Inst. Mech. Eng. Part C* **2009**, *223*, 873–888. [[CrossRef](#)]
14. Long, C.A.; Miles, A.L.; Coren, D.D. Windage Measurements in a Rotor Stator Cavity with Rotor Mounted Protrusions and Bolts. In Proceedings of the ASME Turbo Expo 2012: Turbine Technical Conference and Exposition, Copenhagen, Denmark, 11–15 June 2012.
15. Barabas, B.; Clauss, S.; Schuster, S.; Benra, F.-K.; Dohmen, H.J. Experimental and numerical determination of pressure and velocity distribution inside a rotor-stator cavity at very high circumferential Reynolds numbers. In Proceedings of the 11th European Conference on Turbomachinery, Madrid, Spain, 23–27 March 2015.
16. Will, B.C.; Benra, F.K. Investigation of the Fluid Flow in a Rotor-Stator Cavity with Inward Through-Flow. In Proceedings of the FEDSM2009, ASME Fluids Engineering Conference, Vail, CO, USA, 2–6 August 2009.
17. Will, B.C.; Benra, F.-K.; Dohmen, H.J. Numerical and Experimental Investigation of the Flow in the Side Cavities of a Centrifugal Pump. In Proceedings of the 12th International Symposium on Transport Phenomena and Dynamics of Rotating Machinery, Honolulu, HI, USA, 4–7 April 2010.
18. Will, B.C.; Benra, F.-K.; Dohmen, H.J. Investigation of the Flow in the Side Chambers of a Centrifugal Pump with Volute Casing. In Proceedings of the 10th International Symposium on Experimental Computational Aerothermodynamics of Internal Flows, Brussels, Belgium, 4–7 July 2011.
19. Han, H.; Gao, S.; Li, J.; Zhang, Y. Exploring fluid resistance of disk rotor based on boundary layer theory. *Mech. Sci. Technol. Aerosp. Eng.* **2015**, *34*, 1621–1625.
20. Shi, W.-D.; Wang, H.-L.; Zhou, L.; Zou, P.-P.; Wang, C. The Estimation and Experiment of Axial Force in Deep Well Pump Basing on Numerical Simulation. *Int. J. Mod. Educ. Comput. Sci.* **2010**, *2*, 53–61. [[CrossRef](#)]



© 2017 by the authors. Licensee MDPI, Basel, Switzerland. This article is an open access article distributed under the terms and conditions of the Creative Commons Attribution NonCommercial NoDerivatives (CC BY-NC-ND) license (<https://creativecommons.org/licenses/by-nc-nd/4.0/>).